J Porous Mater (2018) 25:1047–1056
DOI 10.1007/s10934-017-0516-9

Pore size-controlled synthesis of 3D hierarchical porous carbon materials for lithium-ion batteries

Zhiling Li[1] · Ke Zhang[1] · Meng-Yuan Li[1] · Chun-Ling Liu[1] · Wen-Sheng Dong[1]

Published online: 25 October 2017
© Springer Science+Business Media, LLC 2017

Abstract 3D hierarchical porous carbons (3DCs) with different pore size distributions are prepared by using $Ni(OH)_2$ as template. The morphology, crystalline features, pore structure and surface composition of the hierarchical porous carbons are characterized using various analytic techniques including scanning electron microscopy, transmission electron microscopy, N_2 physical adsorption, powder X-ray diffraction and X-ray photoelectron spectroscopy. It is found that the pore size distributions of the 3DCs play an important role in the lithium-storage capacity when they are used as anode materials for rechargeable lithium-ion batteries. The typical sample 3DC-20 has a specific reversible capacity of 630 mAh g^{-1} in the first cycle and and 363 mAh g^{-1} after 50 cycles. The high capacity of 3DC-20 can be attributed to the existence of the largest amount of micropores with 0.6–0.9 nm pore width, which increase the lithium storage capacity; in addition, the existence of mesoporous and macroporous effectively shortens the distance for charge diffusion, the turbostratic graphite structure low resistance for electron conduction.

Keywords Porous carbons · Electrode materials · Lithium-ion batteries

✉ Chun-Ling Liu
clliutt@snnu.edu.cn

✉ Wen-Sheng Dong
wsdong@snnu.edu.cn

[1] Key Laboratory of Applied Surface and Colloid Chemistry (SNNU), MOE, School of Chemistry and Chemical Engineering, Shaanxi Normal University, Xi'an 710062, China

1 Introduction

Among all the energy storage devices, rechargeable lithium-ion batteries (LIBs) are considered to be one of the state-of-the-art power devices for a variety of consumer and military applications. In today's commercial rechargeable LIBs, graphite, one carbonaceous material with the highest graphitization, is almost the only used anode material, due to its cheap cost, highly thermal and chemical stability, low electrochemical potential with respect to lithium metal, and eco-friendliness. However, two major drawbacks i.e. poor rate performance and relatively low storage capacity (theoretically 372 mAh g^{-1}, corresponding to a stoichiometric LiC_6 composition) restrict its applicability in LIBs for both high power and high energy densities, which are the critical enabling technology for the development of electric vehicles (EVs) and hybrid electric vehicles (HEVs) [1–7].

Porous carbon materials have received much attention due to their highly developed pore structure that allows them to have large surface area and fascinating applications in the fields of gas separation, water purification, catalyst supports, sensors, and energy storage and conversion devices. For lithium-ion battery anode materials, much effort has been devoted to the exploration of porous carbon materials in order to increase the lithium-storage capacity. Studies on porous carbon anodes indicate that the existence of both micropores and macropores exerts significant effects on their electronic structure and performance, such as shortened diffusion length for lithium ions and electrons and improved reversible capacity [8–13]. The use of porous carbon in the latter applications requires an optimal combination of high porosity and surface area as well as good transport property. An important trend in the field of porous materials focuses on the generation of hierarchical pore systems [14–16]. Such hierarchical structures are characterized by

the presence of macropores (> 50 nm) along with micropores and mesopores. The presence of macropores is desirable since these bigger pores can act as transport channels for liquids and gases, thus increasing the accessibility of the smaller pores. Fujimoto et al. have deemed that the micropores is not a requirement, since micropores tend to act as deep trap sites, thereby hindering the reversibility of underlying binding processes such as Li insertion [17]. But the existence of micropores can effectively improve the capacity of lithium-ion storage.

In the present study, we prepared 3D hierarchical porous carbon (3DC) with different pore size distributions through changing the amount of template, and investigated their electrochemical performance as electrode materials for lithium-ion batteries. We found that the 3DC containing the largest amount of micropores with size of 0.6–0.9 nm, together with some mesoporous and macroporous revealed good electrochemical performance with much larger specific reversible capacity than the theoretical value of the conventional graphite anode.

2 Experimental

2.1 Preparation

Typically 25 g of $Ni(NO_3)_2{\cdot}6H_2O$ aqueous solution with different concentrations (10, 20, 30 and 40 wt%) was dropped into 50 g of 10 wt% NaOH aqueous solution, and stirred continuously for 4 h for the formation of $Ni(OH)_2$ precipitation. Subsequently, 25 g of 20 wt% ethanol solution of phenolic resin (Phenolic resin 2123, Mw = 2000) was added under strong stirring. The hybrid system was evaporated for 24 h in a glass utensil at 60 °C to obtain the composite of inorganic and resin [13]. The composite was carbonized in a tubular furnace under nitrogen atmosphere. The sample was heated from room temperature to 473 K with a ramping rate of 1 K min^{-1} and remained at 473 K for 2 h, and then was heated to 873 K and remained at 873 K for 4 h. After carbonization, the inorganic template was etched with 3 M HCl solution. The obtained samples were denoted as 3DC-10, 3DC-20, 3DC-30 and 3DC-40, respectively. A reference sample was also prepared using the similar procedure without addition of template, and the obtained sample was denoted C-0.

2.2 Materials characterization

The surface morphology and diameter of the samples were determined using a scanning electron microscopy (SEM, Philips-FEI Quanta 200). The microstructures were characterized using a transmission electron microscopy (TEM, JEOL JEM-2100). For the TEM analysis, a dilute suspension of the sample was dropped onto a carbon-coated TEM grid, and dried. Powder X-ray diffraction (XRD) was performed on a Rigaku D/MAX-III X-ray diffractometer (35 kV, 40 mA) using a Cu*K*α source. The diffraction patterns were taken from 10° to 80° at a scan rate of 8°/min. X-ray photoelectron spectroscopy (XPS) was performed using a VG Scientific (ESCALAB 250) photoelectron spectroscopy. The X-ray source was Al Kα with 1486.6 eV operating at 12 kV and 73 W. The surface area and the pore size distribution (PSD) of the 3DCs were obtained from N_2 (77 K) adsorption measurement using a Micromeritics ASAP2020M system. The PSD was calculated using density functional theory (DFT), and the surface area of the 3DCs was calculated by the Brunauer, Emmett, and Taylor (BET) method. The micropore surface area S_{mi} was obtained using the *t* plot method [18]. The average pore diameter (D) was estimated from the S_{BET} and total pore volume (V) according to the equation D = 4V/S.

2.3 Electrochemical tests

The working electrode with a diameter of12 mm consisted of 80 wt% active material, 10 wt% carbon black, 10 wt% polyterafluoroethylene (PTFE) was prepared by mixing the active material, carbon black, and PTFE emulsion with ethanol to form an electrode paste, then the paste was rolled into ca. 0.1 mm thick film, and finally the electrode film was pressed onto a nickel foam current collector. Lithium foil served as the counter and reference electrode. The electrolyte was1.0 M $LiPF_6$ dissolved in a mixed solution of ethylene carbonate (EC)-dimethyl carbonate (DMC) (1:1, by weight). The cells (CR2032 coin type) were assembled in an argon-filled glove box where both moisture and oxygen levels were less than 1 ppm. They were charged and discharged at a constant current density of 50 mA g^{-1} between cut-off potentials of 0.005 and 2.0 V on a LAND CT2001A cell test apparatus. The impedance spectra were obtained using an Ivium Star electrochemical workstation in a 10.0 mV AC voltage signal in the 100 kHz–10 mHz frequency range in automatic sweep mode from high to low frequency.

3 Results and discussion

3.1 Material characterization

The textural porosities of the synthesized samples were characterized by N_2 adsorption analysis. Figure 1 shows the N_2 adsorption–desorption isotherms. All the samples, except C-0, gave Type IV isotherms with H1 hysteresis, revealing the hierarchical porous structure with open cylindrical pores, which was resulted from the removal of hard template. C0 shows Type I isotherms, which is typical characteristics

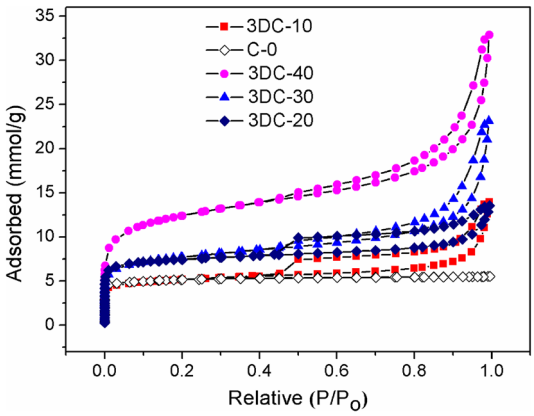

Fig. 1 N_2 adsorption–desorption isotherms of samples

of microporous carbons. Table 1 shows the pore structural parameters. It can be seen that the sample C-0 has a BET surface area of 390.6 $m^2\ g^{-1}$ and total pore volume of 0.19 $m^3\ g^{-1}$; as the addition of $Ni(NO_3)_2{\cdot}6H_2O$ in the preparation procedure increases, the BET surface area, external surface area and total pore volume all increase. This is due to the fact that with increasing the addition of $Ni(NO_3)_2{\cdot}6H_2O$, the formation of $Ni(OH)_2$ template increases; after the removal of NiO or Ni particles derived from pyrolysis of $Ni(OH)_2$ or carbonthermal reduction of NiO by etching with hydrochloric acid the carbon matrix becomes more disarray, then more micropores and mesopores are formed.

The pore-size distribution of these samples is shown in Fig. 2. Five regions can be identified: (I) 0.4–0.6 nm ultrafine micropores, (II) 0.6–0.9 nm ultrafine micropores, (III) micropores (1–2 nm), (IV) mesopores (2–50 nm), (V) macropores (> 50 nm). It can be seen that the sample C-0 has a narrow distribution of microporosity with most pores falling in the region I. In comparisons with C-0, the amount of ultrafine micropores in region I in 3DC-10 decreases; whereas, the amount of ultrafine micropores in region II, micropores in region III, mesopores in region IV and macropores in region V all increase. 3DC-20 exhibits a similar pore-size distribution with 3DC-10, but has larger amount of ultrafine micropores in region II and micropores in region III, lower amount of mesopores in region IV and macropores in region V. 3DC-30 has lower amount of ultrafine micropores in region I and II than 3DC-20, but larger amount of micropores in region III, mesopores in region IV and macropores in region V. With further increasing the addition of $Ni(NO_3)_2{\cdot}6H_2O$ to 40 wt%, the PSD shifts to a larger size; ultrafine micropores in region I and II disappear in 3DC-40, only micropores in region III, mesopores in region IV and macropores in region V are presented.

Figure 3 shows SEM images of the samples. It can be seen that C-0 looks like a monolith with smooth surface, while 3DC-10 exhibits beehive-like structure with many macroporous cores, these cores extend into the particles. With increasing the addition of $Ni(NO_3)_2{\cdot}6H_2O$, the texture of the macroporous cores in the obtained samples is disappeared, and the morphology of the samples changes from big blocks into small fragments.

Figure 4 shows TEM images of the samples. The TEM image of C-0 was not obtained because the electron beam could not penetrate the monolith structure. The TEM images of 3DC-10, 3DC-20, 3DC-30 and 3DC-40 reveal that there exist large amounts of pores in these samples. Figure 4e shows a higher magnification TEM image of 3DC-20. The well-developed turbostratic graphite structure can be clearly observed in the shells. The confined growth of turbostratic graphitic structure within the carbon shell is responsible for the pseudomorphic transformation from polymer to turbostratic graphitic carbon.

Figure 5 shows the XRD patterns of these 3DC samples. As shown in Fig. 5, the diffraction pattern of C-0 shows a broad peak at around 19° due to adjacent chains of linear polymer [19], indicating that the carbon was not carbonized completely. The diffraction patterns of 3DC-10 and 3DC-20 show three peaks at around 25°, 44° and 51°, respectively. The peak at 25° corresponds to the (002) reflection of the turbostratic graphitic crystals, and the peaks at 44°, 51° are caused by Ni particle residues which are wrapped by the carbon and not completely removed by carefully etching with concentrated hydrochloric acid owing to big block structure

Table 1 Pore structure parameters of samples

Samples	BET surface area ($m^2\ g^{-1}$)	Micropore surface area ($m^2\ g^{-1}$)	External surface area ($m^2\ g^{-1}$)	Cumulative surface area in 0.6–0.9 nm pore width ($m^2\ g^{-1}$)	Total pore volume ($m^3\ g^{-1}$)	Micropore volume ($m^3\ g^{-1}$)	Cumulative pore volume in 0.6–0.9 nm pore width ($m^3\ g^{-1}$)
C-0	390.6	323.1	67.5	18.1	0.19	0.15	0.007
3DC-10	405.5	272.3	133.2	27.6	0.39	0.12	0.01
3DC-20	568	424.7	143.6	77.3	0.39	0.19	0.029
3DC-30	597.5	331.6	265.8	67.2	0.58	0.15	0.025
3DC-40	972	467	504	0	0.88	0.21	0

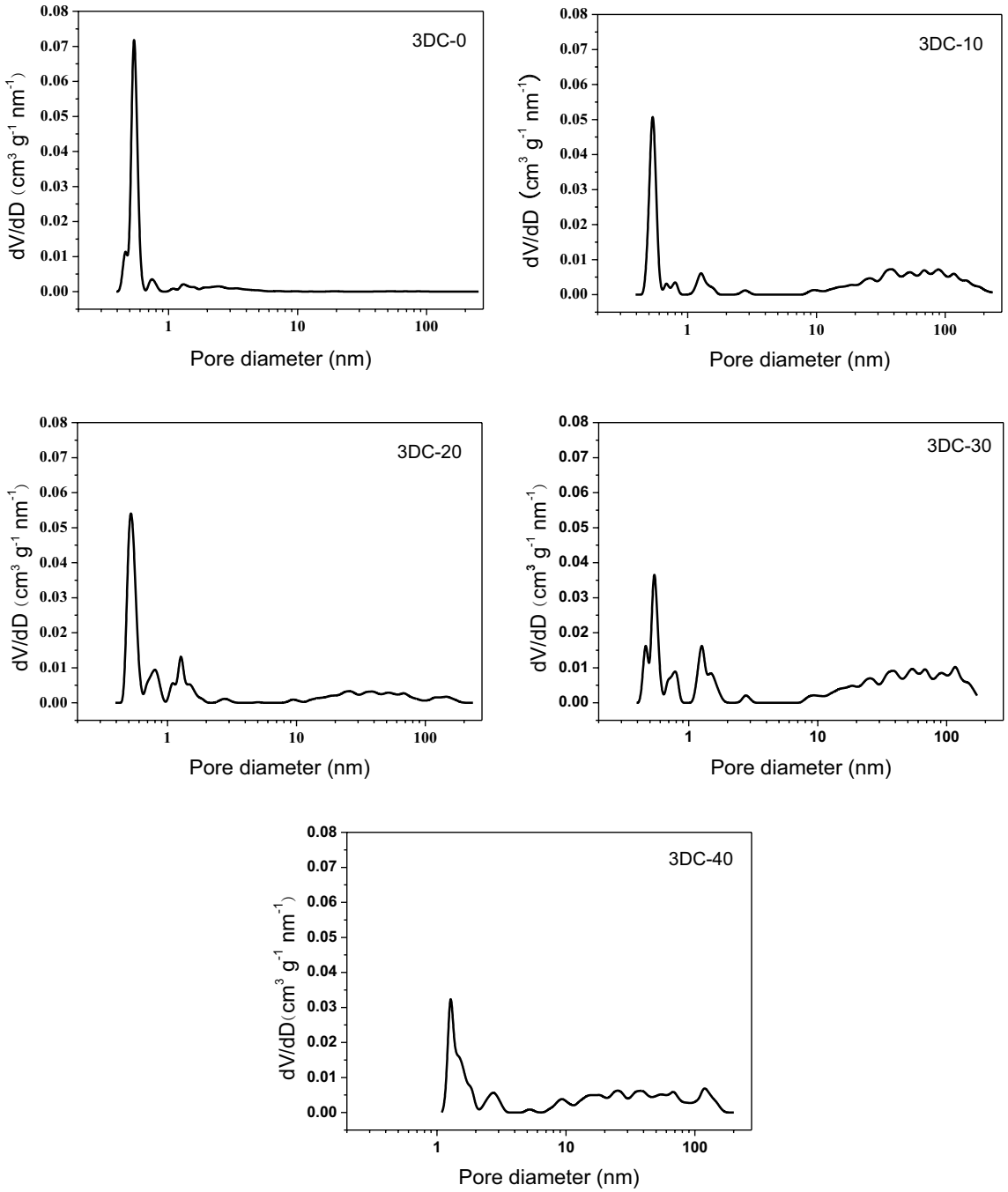

Fig. 2 The pore diameter distribution of samples

for both 3DC-10 and 3DC-20 as confirmed by SEM images. The results suggest that metallic Ni residues could catalyze graphitization of amorphous carbon during carbonization [20]. The diffraction patterns of 3DC-30 and 3DC-40 shows a broad peak around at 22° corresponding to the (002) reflection of amorphous carbon.

The samples were further characterized by XPS and the results are summarized in Table 2. Figure 6 shows a high-resolution C 1s spectra of a typical sample (3DC-20), which exhibits several peaks. Peak area was estimated by calculating the integral of each peak after subtraction of the background and fitting the experimental peak by a Gaussian curve. The binding energy values have been identified as C–C at ~ 284.6 eV, C–O at ~ 286.2 eV, C=O at ~ 287.3 eV, and O–C=O at ~ 289.2 eV. The surface content of O element in 3DC-10, 3DC-20, 3DC-30 and 3DC-40 are 6.42, 7.22,

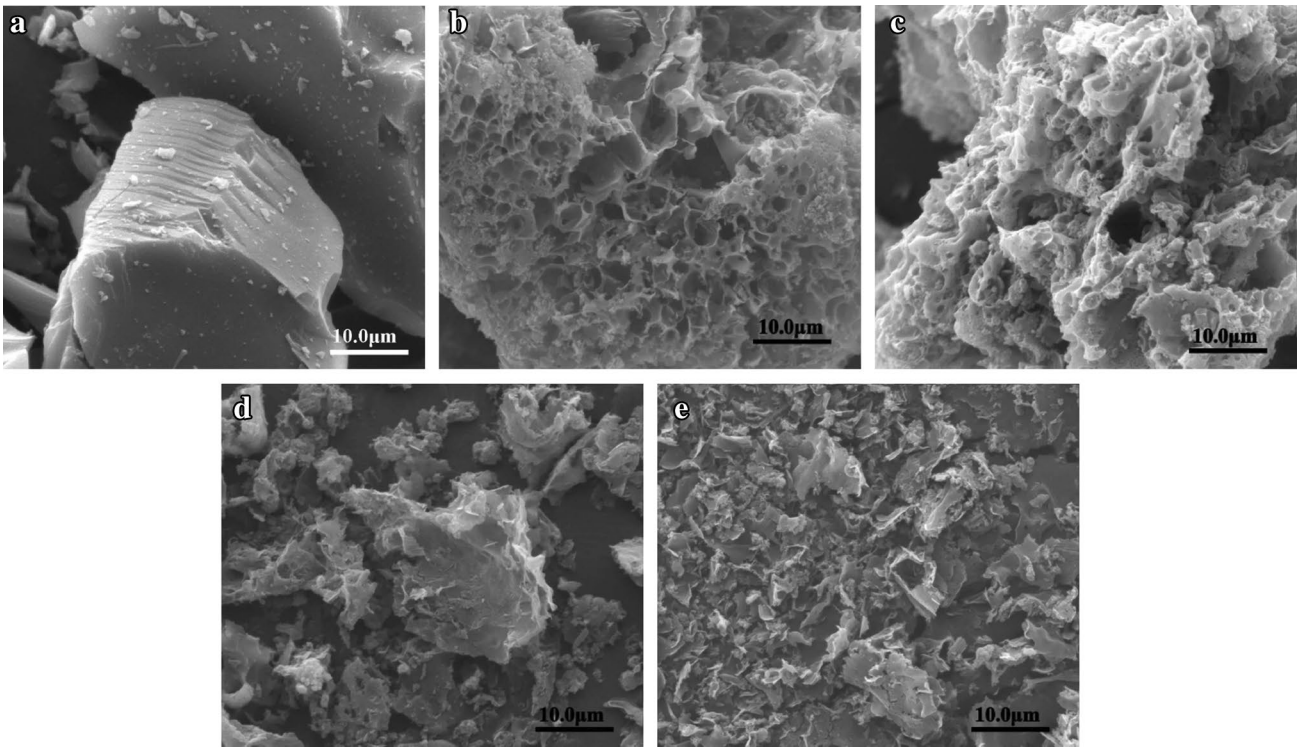

Fig. 3 SEM images of samples: **a** C-0, **b** 3DC-10, **c** 3DC-20, **d** 3DC-30, and **e** 3DC-40

9.26 and 10.57 at%, respectively, indicating that surface oxygen functional groups increase with increasing the content of $Ni(OH)_2$ during 3DC preparation. This may be caused by carbon-thermal reduction of NiO derived from pyrolysis of $Ni(OH)_2$ during carbonization. The surface content of O element in C-0 is 9.22 at%, which is higher than that of 3DC-10 and 3DC-20. This is probable due to that the C-0 sample was not carbonized completely as confirmed by XRD analysis.

3.2 Electrochemical properties

Galvanostatic discharge (Li insertion)—charge (Li extraction) experiments were firstly carried out at a current density of 50 mA g^{-1} within a voltage window of 0.005–2.0 V to evaluate the electrochemical performance of the samples. The first-two discharge–charge curves of the samples are shown in Fig. 7. The first discharge curves of the samples have a plateau in the range of 0.6–1.0 V, corresponding to the electrolyte decomposition and the formation of solid electrolyte interface (SEI) film on the surface of carbon, which causes large irreversible capacity. The length of this plateau increases with increasing the addition of $Ni(NO_3)_2{\cdot}6H_2O$ during the preparation. This is due to that the increase of specific surface area of 3DCs provides more active sites for the reaction of the electrolyte decomposition and the formation of SEI film [9]. During the second discharging process, these discharging curves do not show any plateau at 0.7–1.0 V for all the samples, confirming that the reaction of the electrolyte decomposition and the formation of SEI film occur only in the first cycles. The plateaus in the voltage range of 0–0.5 V in the first discharge curves of 3DCs can be attributed to the insertion of Li into the carbon materials.

The data in Fig. 7 reveals that the specific reversible capacities of C-0, 3DC-10, 3DC-20, 3DC-30, and 3DC-40 in the first cycle are 323, 470, 630, 409 and 355 mAh g^{-1}, respectively, which corresponds to the first coulombic efficiency of 25, 31, 33, 19 and 17%. The first coulombic efficiencies of 3DCs are very low, after three cycles the coulombic efficiency increases to above 95%.

The reversible capacity *vs*. cycle number profiles of the samples are illustrated in Fig. 8. In the fifty cycles, the 3DCs electrodes are stable. 3DC-20 has a specific reversible capacity of 630 mAh g^{-1} in the first cycle and 363 mAh g^{-1} after 50 cycles. The 3D hierarchical porous carbons exhibited comparable electrochemical performance with many other amorphous carbons [21–23]. For example, polystyrene-derived carbon with hierarchical macro–meso–microporous structure prepared by Yang et al. [21] attained a stable capacity of 410 mAh g^{-1} at a current density of 100 mA g^{-1} for over 100 cycles. The activated hierarchical porous carbon supporting poly(1,5-diamino-anthraquinone) cathode

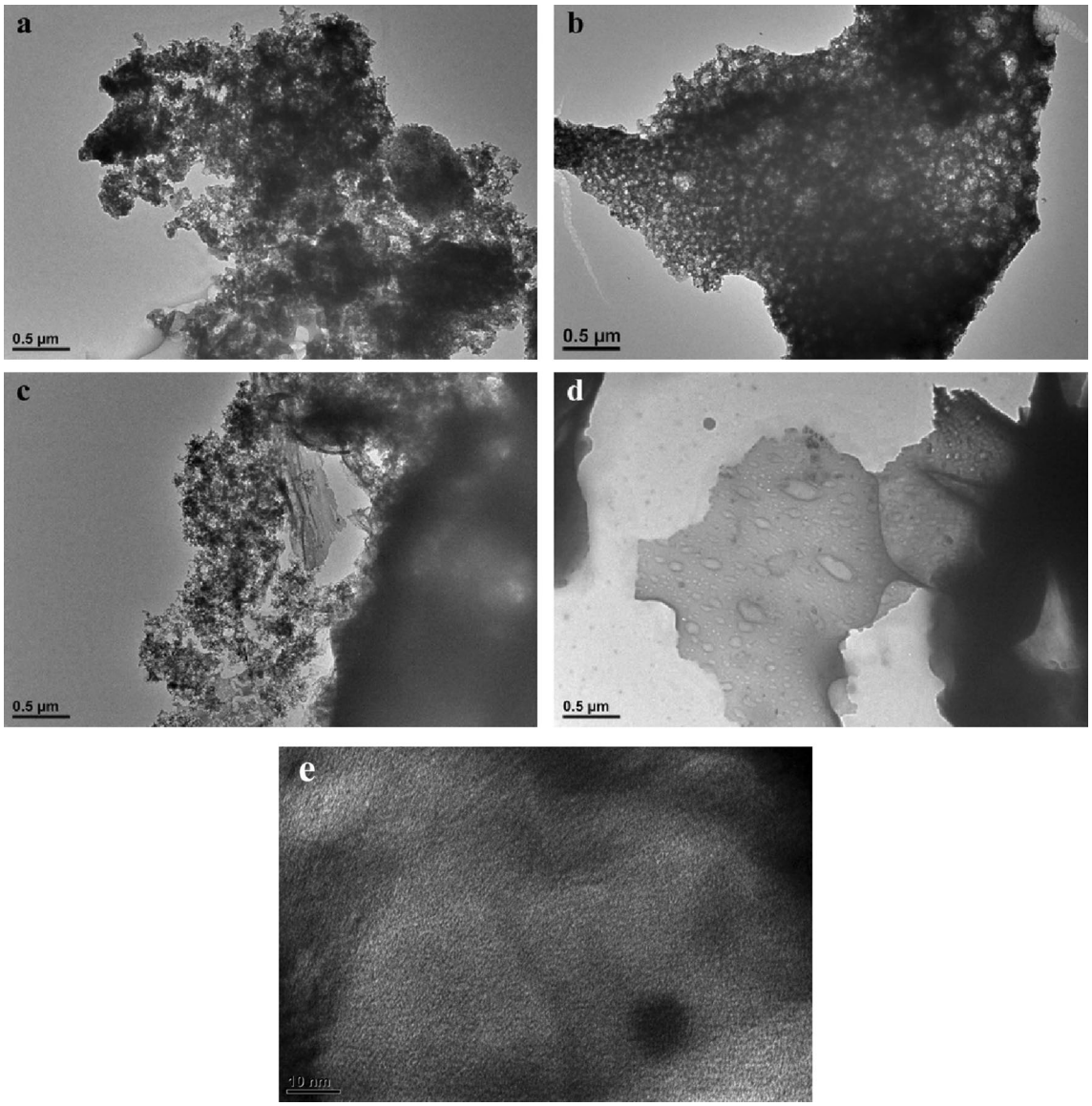

Fig. 4 TEM images of samples: **a** 3DC-10, **b** 3DC-20, **c** 3DC-30, **d** 3DC-40, **e** the HRTEM image of 3DC-20

prepared by Tao et al. [22] achieved a discharge capacity of 250 mAh g^{-1} at the current density of 100 mA g^{-1}. The morphous and turbostratic porous carbon spheres prepared by Etacheri et al. [23] revealed a discharge capacity of 378 mAh g^{-1} at a current density of 0.1 C (37.2 mA g^{-1}). At a higher charge–discharge rate of 1 C, the turbostratic carbon spheres exhibited a reversible specific capacity of 270 mAh g^{-1}. After 100 charge–discharge cycles at current densities of 0.1 C and 1 C, carbon spheres retained stable specific capacities of 365 and 250 mAh g^{-1}, respectively.

The reversible capacities of the samples in the fifty cycles change following the order: 3DC-20 > 3DC-10 ~ 3DC-30 > 3DC-40 > C-0. The results can be explained reasonably as follows.

The difference between the reversible capacities of the samples is close related with their pore structures. As can be seen from Fig. 2, C-0 has the largest amount of ultrafine micropores in region I (0.4–0.6 nm), but small amount of ultrafine micropores in region II (0.6–0.9 nm); while 3DC-40 has the largest amount of micropores in region III (1–2 nm) and mesopores in regions IV (2–50 nm) but no micropores in region II. Both of them have poor capacity, indicating that these pores in regions I, III and IV are not efficiency for Li insertion capacity. The cumulative surface

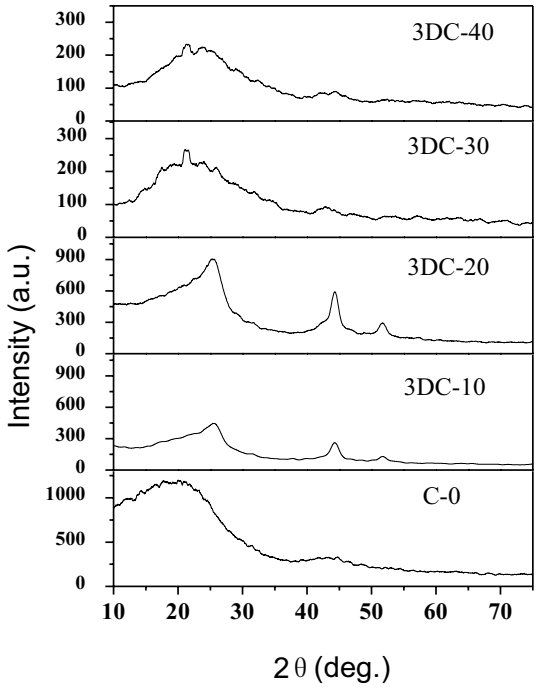

Fig. 5 XRD patterns of the samples

area and pore volume of the samples in the pore size range of 0.6–0.9 nm shown in Table 1 indicate that 3DC-20 has the largest amount of micropores in region II, followed by 3DC-30 and 3DC-10. These three samples reveal higher reversible capacity than 3DC-40 and C-0, and among them 3DC-20 reveals the highest reversible capacity. This result suggests that the micropores in region II are more efficiency for Li insertion capacity than those pores in regions I, III and IV. Similar behavior was also observed by Winter and co-workers [24, 25]. There are several models for excess Li capacity ($x > 1.0$ for Li_xC_6) observed in carbonaceous materials, including formation of lithium multi-layers on graphene sheets [26], Li_2 covalent molecules [27], Li–C–H bonds [28], and metallic lithium clusters in microcavities [1, 2]. Ultramicropores with size of 0.7–0.9 nm surrounded by small graphite stacking blocks are assumed to be able to trap lithium in a metal lithium cluster [24, 25].

Although 3DC-30 have larger amount of micropores in region II than 3DC-10, but the average reversible capacity of these two samples are similar, a possibly reason is that relative larger amount of surface oxygen functional groups in 3DC-30 cause irreversible capacity and reduce the reversible capacity at the same time. 3DC-10 has a little bit larger amount of micropores in region II but much higher reversible capacity than C-0. Probably in this case the larger amount of mesopores and macropores in 3DC-10 also play important roles as macropores may serve as ion-buffering reservoirs, mesoporous walls with smaller ion-transport resistance. In another words, the existence of mesopores and macropores could shorten the distance for charge diffusion, low resistance for electron conduction.

AC impedance spectroscopy was further employed to analyze the performance of the batteries made from these samples. Figure 9 presents the Nyquist plots of the electrodes. Z' and Z'' are the real and imaginary parts, respectively, of the complex impedance Z. For each sample, the Nyquist plots are characterized by a semicircle at high frequency range and a straight line in the low frequency range. According to the previous paper [29, 30], the semicircle at high frequency range is attributed to the contact resistance and charge-transfer impedance, the straight line in the low frequency range is assigned to the lithium diffusion process within electrode.

These AC impedance spectra for the composite electrodes can be modeled by an equivalent circuit, which is presented in Fig. 10. R_s is the electrolyte resistance, R_{ct} is the charge-transfer resistance, C_{dl} is the double-layer capacitance, and Z_w is the Warburg impedance related to the diffusion of lithium ions into the carbon electrodes. The mass-normalized resistances (in Ω g units) obtained from impedance spectra of electrodes are summarized in Table 3. It can be seen that the R_s of these electrodes are roughly identical, indicating that they have approximately electric conductivity. The *R*ct values of the samples used in the present study are believed to reflect the penetration of

Table 2 XPS data of samples

Samples	Surface O atomic content (%)	Surface C species relative content (%)			
		C–C 284.8 (eV)	C–O 286.2 (eV)	C=O 287.3 (eV)	O–C=O 289.2 (eV)
3DC-0	9.22	83.57	8.78	3.26	4.4
3DC-10	6.42	78.75	6.87	3.9	10.48
3DC-20	7.22	72.38	9.38	7.11	11.31
3DC-30	9.26	74.83	10.58	7.17	7.42
3DC-40	10.57	73.34	9.81	9.65	7.2

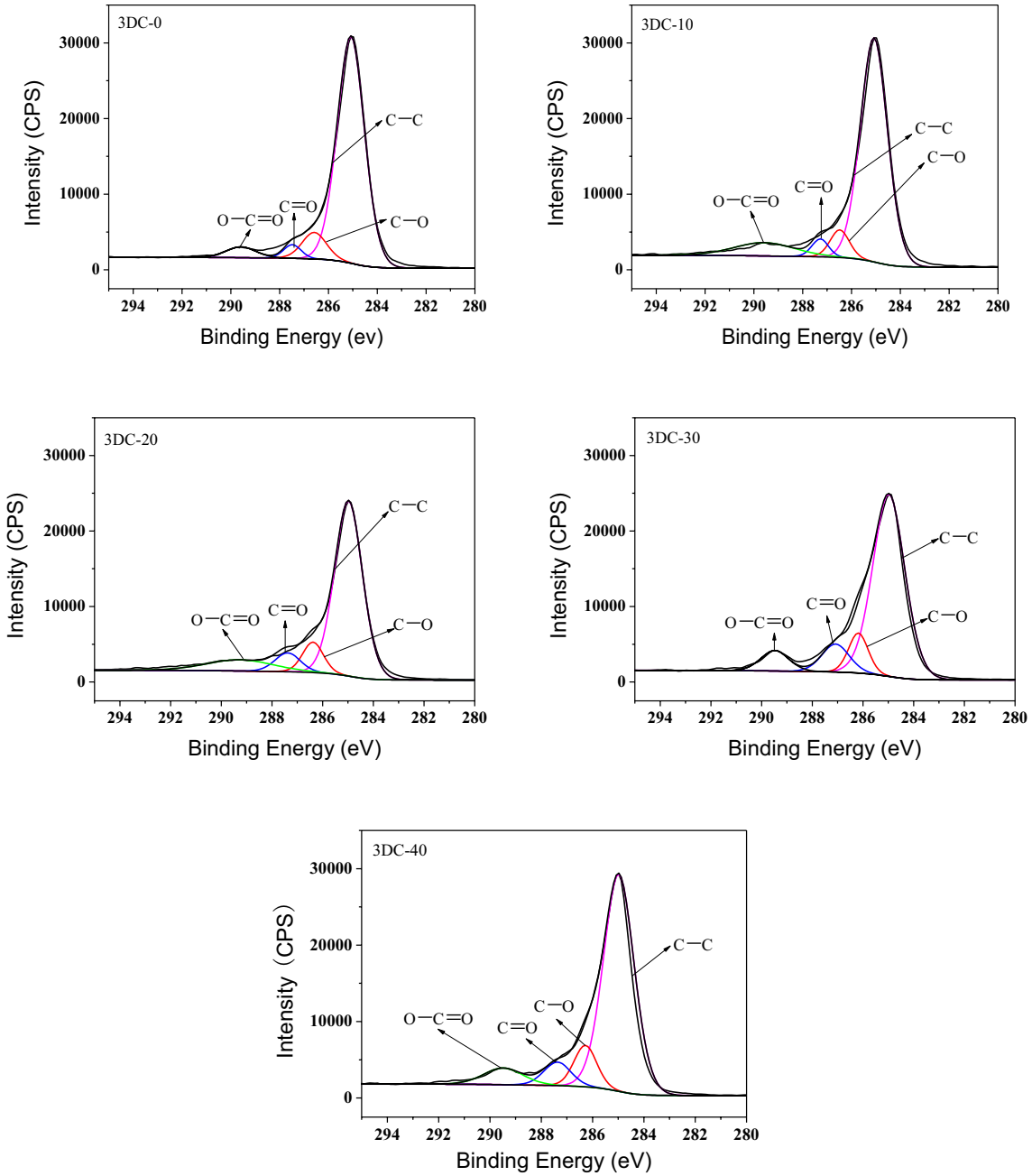

Fig. 6 C 1s XPS spectra of the samples

the electrolyte into the pores of the samples. The relationship between the pore diameter and the resistance has been studied by other authors in previous works [9, 10, 31], and they have concluded that the existence of mesopores and macropores is effective to shorten the distance for charge diffusion, low resistance for electron conduction; but the existence of micropores might act as deep trap sites, and hinder the electrolyte penetration and ionic diffusion to some extent. From Table 3, it can be observed that the R_{ct} values of 3DCs increase in the sequence of 3DC-30, 3DC-20, 3DC-10, C-0, and 3DC-40. Although the 3DC-40 has the largest mesoporous volume, they also has the largest microporous volume which enlarge the R_{ct}, it exhibits the highest R_{ct} value.

4 Conclusions

3D hierarchical porous carbons with different pore size distributions were prepared using $Ni(OH)_2$ template. The pore

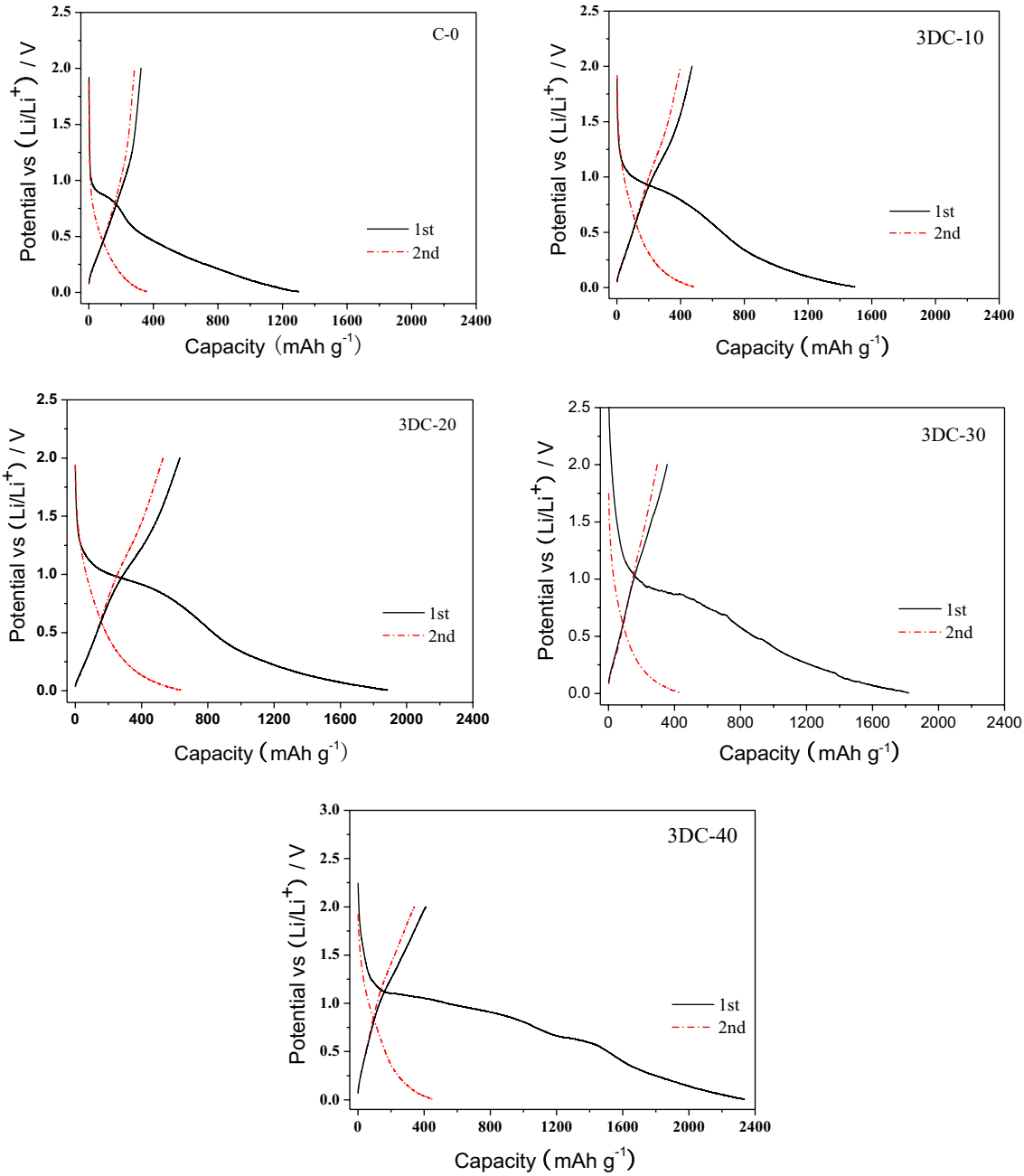

Fig. 7 The first-two charge–discharge curves of samples at the current density of 50 mA g^{-1}

size distributions of the hierarchical porous carbons were controlled through changing the amount of template. It was found that the pore size distributions of the 3DCs play an important role in the lithium-storage capacity. The micropores with size of 0.6–0.9 nm are confirmed to be able to promote effectively the lithium storage capacity. The typical sample 3DC-20 shows a good electrochemical performance with a specific reversible capacity of about 630 mAh g^{-1} in the first cycle and 363 mAh g^{-1} after 50 cycles. The good electrochemical performance of 3DC-20 can be attributed to the existence of the largest amount of micropores with size of 0.6–0.9 nm which increase the lithium storage capacity; inaddition the existence of mesoporous and macroporous effectively shortens the distance for charge diffusion, the turbostratic graphite structure low resistance for electron conduction.

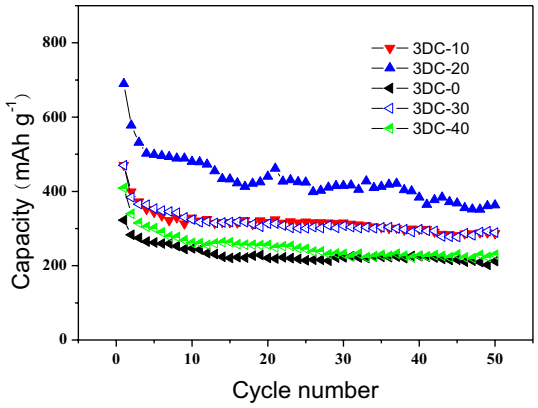

Fig. 8 The reversible capacity versus cycle number profiles of samples at the current density of 50 mA g^{-1}

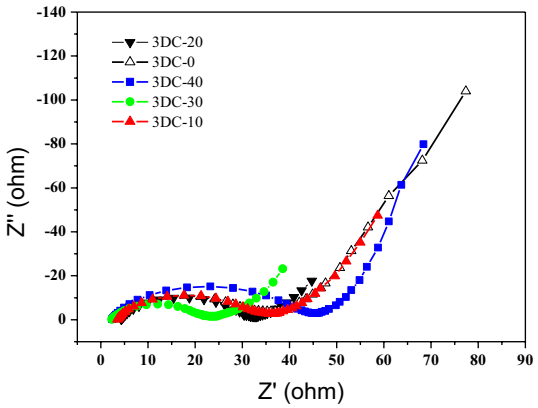

Fig. 9 EIS spectra of samples

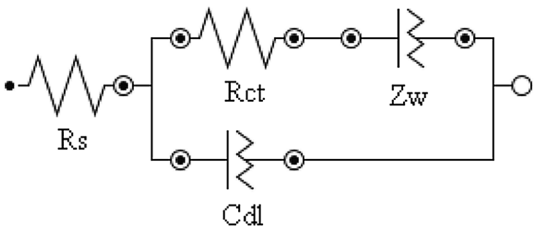

Fig. 10 Equivalent circuit used for the fitting of the spectra

Table 3 Mass-normalized resistances (in Ω g units) obtained from impedance spectra of electrodes

Samples	C-0	3DC-10	3DC-20	3DC-30	3DC-40
R_s (Ω)	2.32	2.31	2.27	2.24	2.48
R_{ct} (Ω)	33.1	31.7	27.3	20.3	42.8

Acknowledgements This work was financially supported by the Program for Key Science and Technology Innovation Team of Shaanxi Province (2012KCT-21), the Fundamental Research Funds for the Central Universities (GK201501007).

References

1. M. Armand, J.M. Tarascon, Nature **451**, 652 (2008)
2. P.G. Bruce, B. Scrosati, J.M. Tarascon, Angew. Chem. Int. Ed **47**, 2930 (2008)
3. Y.G. Guo, J.S. Hu, L.J. Wan, Adv. Mater. **20**, 2878 (2008)
4. J. Maier, Nat. Mater. **4**, 805 (2005)
5. M. Patel, A.J. Bhattacharyya, Electrochem. Commun. **10**, 1912 (2008)
6. Y.P. Wu, E. Rahm, R. Holze, J. Power Sources **114**, 228 (2003)
7. X.L. Wu, Q. Liu, Y.G. Guo, W.G. Song, Electrochem. Commun. **11**, 1468 (2009)
8. J. Lee, J. Kim, T. Hyeon, Adv. Mater. **18**, 2073 (2006)
9. H. Zhou, S. Zhu, M. Hibino, I. Honma, M. Ichihara, Adv. Mater. **15**, 2107 (2003)
10. L. Ji, X. Zhang, Nanotechnology **20**, 155705 (2009)
11. F. Cheng, Z. Tao, J. Liang, J. Chen, Chem. Mater. **20**, 667 (2008)
12. F. Zhang, K.X. Wang, G.D. Li, J.S. Chen, Electrochem. Commun. **11**, 130 (2009)
13. D.W. Wang, F. Li, M. Liu, G.Q. Lu, H.M. Cheng, Angew. Chem. Int. Ed **47**, 373 (2008)
14. T.R. Pauly, Y. Liu, T.J. Pinnavaia, S.J.L. Billinge, T.P. Rieker, J. Am. Chem. Soc. **121**, 8835 (1999)
15. N. Ishizuka, H. Minakuchi, K. Nakanishi, N. Soga, H. Hagayama, K. Hosoya, N. Tanaka, Anal. Chem. **72**, 1275 (2000)
16. Z.Y. Yuan, B.L. Su, J. Mater. Chem. **16**, 663 (2006)
17. H. Fujimoto, A. Mabuchi, K. Tokumitsu, T. Kasuh, J. Power Sources **54**, 440 (1995)
18. B.C. Lippens, J.H. de Boer, J. Catal **4**, 319 (1965)
19. C.L. Liu, W.S. Dong, J.R. Song, L. Liu, Mater. Sci. Eng. A **459**, 347 (2007)
20. A. Oya, S. Yoshida, J. Alcaniz-Monge, A. Linares-Solano, Carbon **33**, 1085 (1995)
21. M. Winter, J.O. Besenhard, M.E. Spahr, P. Novák, Adv. Mater. **10**, 725 (1998)
22. M. Winter, J.O. Besenhard, in *Lithium Ion Batteries: Fundamentals and Performance*, ed. by M. Wakihara, O. Yamamoto (Wiley-VCH, Weinheim, 1988)
23. X. Yang, C. Li, G. Zhang, C. Yang, J. Mater. Sci. **50**, 6649 (2015)
24. T. Zhang, H. Li, Q. Tang, M. Sun, G. Wang, J. Solid State Electrochem. **20**, 2169 (2016)
25. V. Etacheri, C. Wang, M.J. O'Connell, C.K. Chan, V.G. Pol, J. Mater. Chem. A **3**, 9861 (2015)
26. R. Yazami, M. Munshi, in *Handbook of Solid State Bateries and Capacitors*, ed. by M. Munshi (World Scientific, Songapore, 1995), p. 25
27. K. Sato, M. Noguchi, A. Demachi, N. Oki, M. Endo, Science **164**, 556 (1994)
28. J. Dahn, T. Zhang, Y. Liu, J. Xue, Science **270**, 590 (1995)
29. C.L. Liu, W.S. Dong, G. Cao, J. Song, L. Liu, J. Electrochem. Soc. **155**, F1 (2008)
30. S. Yang, H. Song, X. Chen, Electrochem. Commun. **8**, 137 (2006)
31. C.L. Liu, W.S. Dong, G.P. Cao, J.R. Song, Q.G. Guo, L. Liu, Y.S. Yang, J. Electrochem. Soc. **155**, F124 (2008)